Mesoporous Spinel LiMn$_2$O$_4$ Nanomaterial as a Cathode for High-Performance Lithium Ion Batteries

Bo-Mi Hwang[1], Si-Jin Kim[1], Young-Woo Lee[1], Biao Han[1,2], Seong-Bae Kim[1,2], Woo-Seong Kim[2], and Kyung-Won Park[1,*]

[1] Department of Chemical Engineering, Soongsil University, Seoul 156-743, Republic of Korea
[2] Daejung Energy Materials, 740-49, Sinheung-dong, Iksan, Jeonbuk 570-140, Republic of Korea
[*]E-mail: kwpark@ssu.ac.kr

We demonstrate mesoporous spinel LiMn$_2$O$_4$ nanomaterial (NS-LMO) synthesized by polymer template method for high-performance lithium ion batteries. The as-synthesized NS-LMO exhibits complete spinel LMO structure with dominant {111} surfaces, nanocrystalline of ~30 nm in size, and relatively high surface area (~13.8 m^2 g^{-1}) with mesoporous characteristics. In contrast, the LMO (SS-LMO) prepared by the solid state reaction method consists of a spinel structure of LMO and an extra phase of Mn$_2$O$_3$. The NS-LMO displays much higher capacity of ~96.19 mAh g^{-1} at 1 C compared to the SS-LMO (~57.03 mAh g^{-1}) and improved rate cycling performance with the complete capacity retention.

1. INTRODUCTION

Lithium ion batteries (LIBs) have attracted much attention as power sources for various portable electronic devices because of their high energy density [1-4]. Most widely used cathode material is LiCoO$_2$. However, many researchers investigated on several other materials such as LiNiO$_2$, LiMnO$_2$, LiMn$_2$O$_4$ and LiFePO$_4$ [5]. Moreover, the cubic spinel lithium manganese oxide (LiMn$_2$O$_4$, LMO) is the promising candidate as a cathode capable of replacing LiCoO$_2$ in LIBs because of its low cost, high energy density, high thermal stability, and nontoxicity [6,7]. Kim *et al*. reported a spinel-structured LMO by developing a truncated octahedral structure in which most surfaces are aligned to the crystalline orientations with minimal Mn dissolution, while a small portion of the structure is truncated along the orientations to support Li diffusion and thus facilitate high

discharge rate capabilities [8]. Bruce and co-workers synthesized a stoichiometric LMO nanostructured cathode synthesized by a one-pot resorcinol-formaldehyde route with a high initial capacity, excellent rate capacity, and stable cycling performance [9]. Sun *et al*. suggested spinel LMO powders as a cathode with submicron, monodispersed, and highly homogeneous particles for lithium polymer batteries [10].

The electrochemical performances of electrode materials are highly influenced by the particle size, morphology, phase crystallinity, and distribution. In particular, nanostructured electrode materials shorten lithium ion diffusion path and improve a cycling performance of LIBs [11-14]. In general, the spinel LMO has been synthesized by traditional solid-state reaction method that involves mechanical lithium and manganese salts followed by high-temperature calcination owing to the low reactivity of the starting materials. Also, the as-synthesized particles might have impurity phases, inhomogeneity, irregular morphology large particle size and broad particle size distribution [15,16]. In order to overcome these disadvantages and prepare the complete LMO for LIBs, several soft chemical approaches have been performed using sol-gel method [17-19], combustion process [20,21], chemical precipitation [22], and hydrothermal method [23,24], Navulla *et al*. prepared a lithium-manganese cathode material by simple one-step solid-state reactions at 600 ^{o}C using single-source precursor [25]. Ding *et al*. demonstrated single-crystalline spinel LMO nanotubes synthesized via template-engaged reaction at 700 ^{o}C for high-power LIBs [26]. Patey *et al*. produced LMO nanoparticles by a one-step flame spray pyrolysis process [27]. Luo *et al*. demonstrated well-ordered mesoporous spinel LMO prepared by annealing the lithiated mesoporous MnO_2 at a low temperature of 350 ^{o}C [28]. Recently, a polymer template method using the triblock copolymer as a soft template has been used for preparing a variety of mesoporous oxide nanomaterials [29,30]. However, there are few reports on the synthesis of nanostructure electrodes for LIBs using the polymer template method.

In general, conventional LMO that prepared at low-temperature has almost polycrystalline or low crystalline with impurity. The excellent crystallinity of the LMO could improve the electrochemical performance by impeding manganese dissolution from the spinel material into the electrolyte [31]. Herein, we synthesized mesoporous LMO cathode nanomaterials with a complete spinel structure for LIBs using a polymer template method at a relatively low temperature of 500 ^{o}C (Scheme 1). The structural characterization of the LMO was carried out using wide-angle X-ray diffraction (WA-XRD), field emission scanning electron microscopy (FE-SEM), and field emission transmission electron microscopy (FE-TEM). The surface area of the electrodes was analyzed by a nitrogen sorption measurement. To evaluate the performance for LIBs, charge-discharge, rate cycling, and electrochemical impedance spectroscopy (EIS) curves of the electrodes and were obtained using a lithium coin cell.

2. EXPERIMENTAL

Nanostructured $LiMn_2O_4$ (NS-LMO) was synthesized by the polymer template (PT) method (Scheme 1(a)). Poly(ethylene glycol)–poly(propylene glycol)–poly(ethylene glycol) (P-123, 10 g) and of lithium dodecyl sulfate (98.5% purity, Aldrich, 0.45 g) were dissolved in 102.4 ml of cyclohexane

(99.5%, Aldrich) and 12.4 ml of 1-butanol (99.4%, Aldrich) until perfectly transparent. Aqueous solutions of lithium nitrate (LiNO$_3$, 99%, Aldrich) and manganese nitrate (Mn(NO$_3$)$_2$, 99.99%, Aldrich) were prepared using distilled water as a solvent and 10 ml of 1 M LiNO$_3$ and 2 M Mn(NO$_3$)$_2$ was added to non-aqueous polymer medium. After stirring for 24 h, the solution became a white emulsion and the emulsion was evaporated at 125 ^{o}C in silicon oil bath for 8 h until a black gel was obtained. The obtained gel was heated at 300 ^{o}C in air for 6 h to get the precursor. The precursor was ground to a fine powder and calcined at 500 ^{o}C in air for 6 h to obtain final product.

Bulk-type LiMn$_2$O$_4$ (SS-LMO) was synthesized by the conventional solid-state reaction (SSR) method (Scheme 1(b)). 0.9 g of lithium acetate dehydrate (63%, Aldrich) and 3.9 g of manganese(II) acetate tetrahydrate (99%, Aldrich) were mixed in stoichiometric amount after physical grinding. The starting materials of lithium and manganese salts as solid–state powders were physically mixed using mortar and pestle. The mixed powder was heated at 300 ^{o}C in air for 6 h and then kept at 500 ^{o}C in air for 6 h.
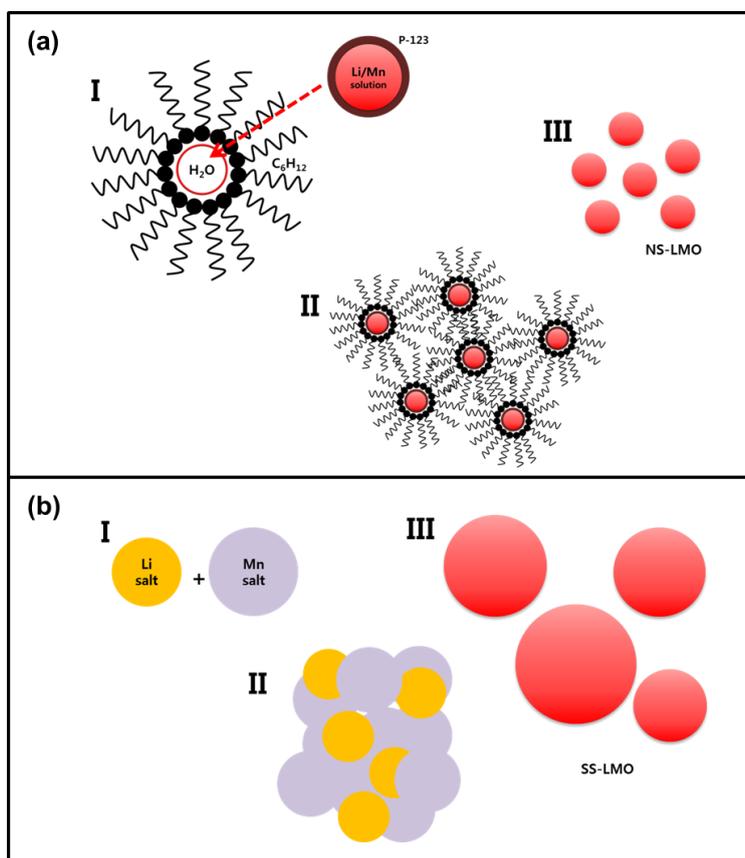

Scheme 1. Schematic representation of synthsis of NS-LMO using PT method and SS-LMO using SSR method.

The samples were characterized by XRD using a D2 phase system with a Cu K$_\alpha$ radiation source of $\lambda = 0.15418$ nm at 30 kV and 10 mA. The XRD data was collected in the 2θ between 10° and 80° with scan rate 4° min^{-1}. The morphology and structure were obtained FE-SEM using a JSM-6700F

system and FE-TEM using a Tecnai G2 F30 system operating at 300 kV. Nitrogen adsorption and desorption isotherms were measured at 77 K using a Micromeritics ASAP 2020. Before the adsorption measurements, all samples were outgassed at 473 K for 6 h in the port of the adsorption analyzer. The starting relative pressure was 0.995 P/P^o and ending relative pressure was 0.01 P/P^o.

The electrochemical performance of the electrodes was determined with 2032 coin-type cells. For preparing working electrodes, a mixture of the active material, acetylene black, and polyvinylidene fluoride binder at a weight ratio of 7:1:2 was pasted on aluminum foil. After vacuum drying at 100 ^{o}C for 12 h, the foil was cut into circular disk with a diameter of 13 mm. The counter electrode was used pure lithium foil which was cut into ϕ16 mm round disk. The electrolyte was 1 M LiPF$_6$ dissolved in a 1:1 (v/v) mixture of ethylene carbonate and diethyl carbonate. The cell was assembled in an argon-filled glove box and tested using charge-discharge system in the voltage range of 3.0-4.3 V vs. Li$^+$/Li at different current density. For EIS analysis, the excitation potential applied to the cells was 5 mV in the frequency ranged between 100 kHz and 10 mHz at full charge at 1 C. All the electrochemical measurements were carried out at 25 ^{o}C.

3. RESULTS AND DISCUSSION
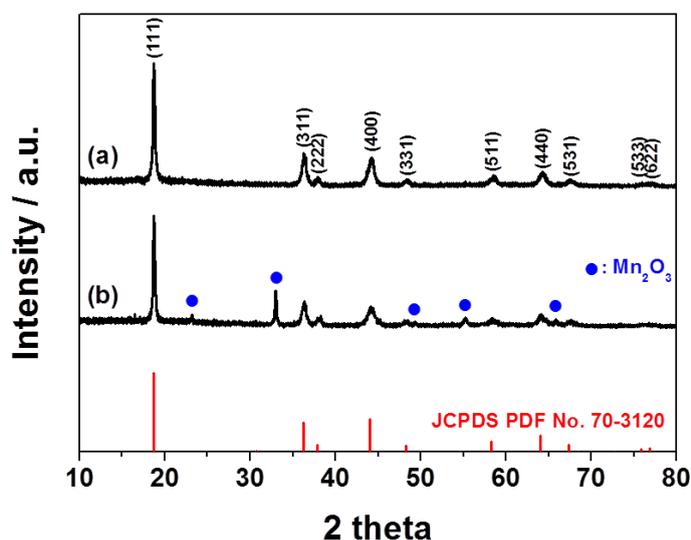
Figure 1. XRD patterns of (a) NS-LMO and (b) SS-LMO.

Fig. 1 shows XRD patterns of the NS-LMO synthesized by the PT method and the SS-LMO prepared by the SSR method. The diffraction peaks of the NS-LMO at 18.7°, 36.2°, 44.0° and 64.0° correspond to (111), (311), (400), and (411), respectively, which is in exact agreement with those of a single-phase spinel LMO material with *Fd3m* space group (JCPDS No. 70-3120) with no peaks of the Mn$_2$O$_3$ phase detected. In contrast, the SS-LMO consists of main LMO phase and Mn$_2$O$_3$ as an impurity as indicated in the Fig. 1. Furthermore, the relative ratio of (111) to (400) for the NS-LMO (~1.85) is much larger than that for the SS-LMO (~1.49), indicating that the NS-LMO has a dominant

plane of (111). Based on the Scherrer equation, the average particle sizes of NS-LMO and SS-LMO are ~29.4 and ~33.5 nm, respectively. This represents that the present synthesis route (PT method) is considerably suitable for preparing a complete LMO nanostructure at low temperature [32].
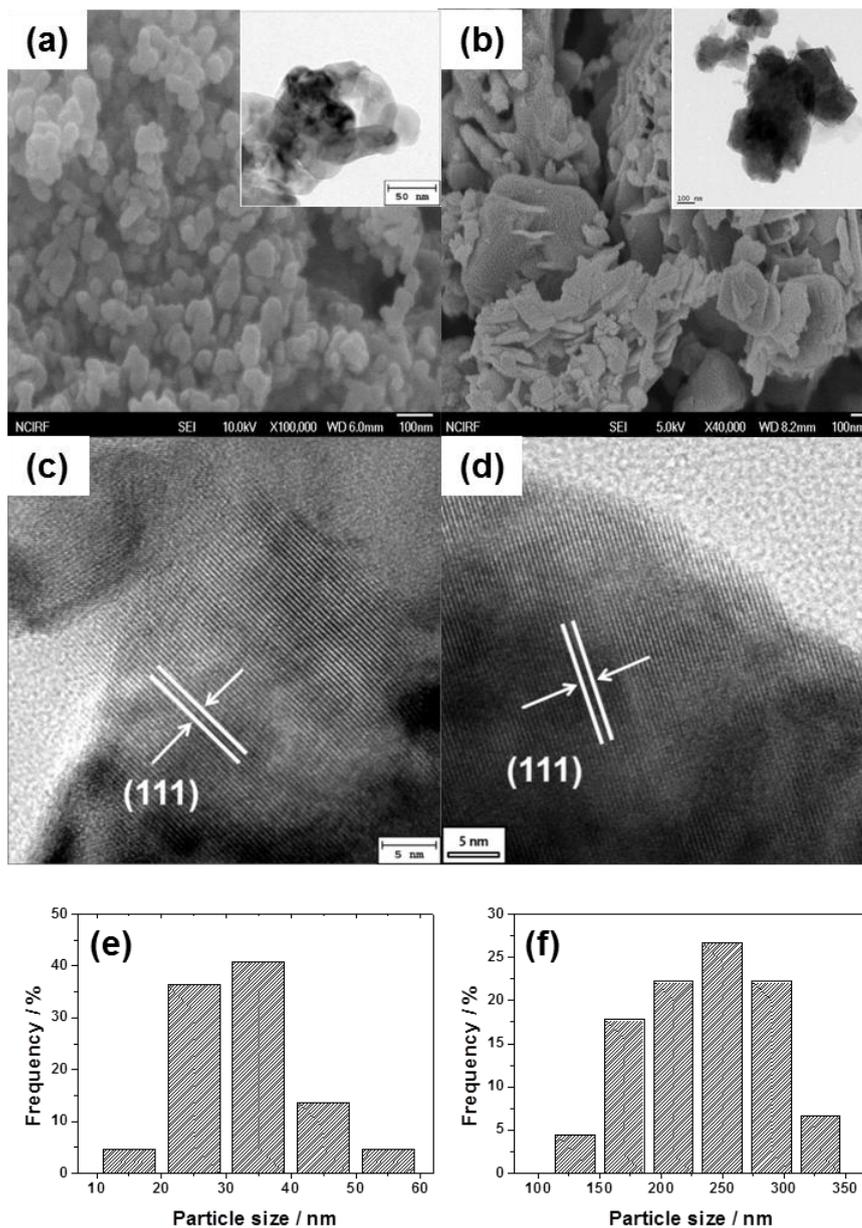
Figure 2. XRD patterns of FE-SEM images [The inset indicates FE-TEM images] of (a) NS-LMO and (b) SS-LMO. HR-TEM images of (c) NS-LMO and (d) SS-LMO. Size distributions of (e) NS-LMO and (f) SS-LMO.

As displayed in the FE-SEM and FE-TEM images in Fig. 2(a), the NS-LMO exhibits a relatively regular structure with a uniform particle size. In contrast, as indicated in Fig. 2(b), the SS-LMO has irregular morphology and size distribution due to an agglomeration between particles. Representative high-resolution TEM (HR-TEM) image (Fig. 2(c)) of the NS-LMO demonstrates

crystalline structure with dominant {111} surfaces having a lattice distance of 0.475 nm. The HR-TEM image (Fig. 2(d)) of the SS-LMO shows {111} surfaces having a lattice distance of 0.475 nm. Sun *et al.* suggested the formation of a solid electrolyte interface on the surface of {111} planes of LMO is critical for stabilizing its crystal structure during lithium ion insertion/desertion process compared to other facets [33]. Also, Kim *et al.* reported the dominant {111} surfaces to minimize the Mn dissolution, exhibiting a superior cycle life and facilitating high discharge rate capabilities [8]. The NS-LMO holds ~31.0 nm in an average size according to the size distribution of the Fig. 2(e), which is in a good agreement with that measured by XRD analysis. The close agreement exhibits that single, non-aggregated, crystalline, pure LMO nanoparticles can be produced by the PT method. In contrast, the SS-LMO exhibits much larger particle size of ~302.1 nm than that of the NS-LMO (Fig. 2(f)). The large difference of the measured particle size of the SS-LMO indicates that aggregated LMO particles with impurities might be obtained by the SSR method.
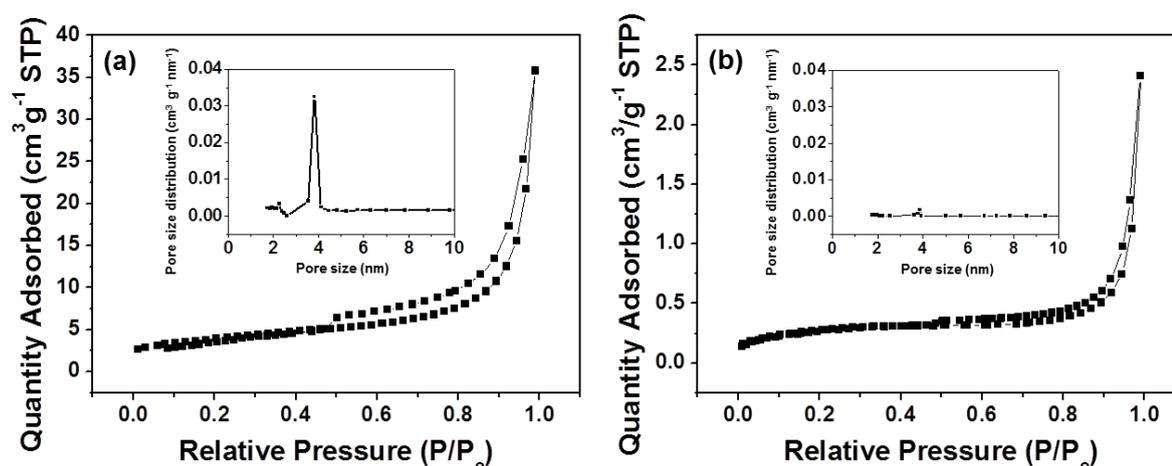
Figure 3. Nitrogen adsorption/desorption isotherms for (a) NS-LMO and (b) SS-LMO. The insets are pore size distributions of the samples.

The nitrogen-adsorption isotherms of the as-prepared LMOs are shown in Fig.3. The LS-LMO exhibits mesoporous structure with ~13.8 m^2 g^{-1} in Brunauer-Emmett-Teller (BET) specific surface area and ~3.8 nm in pore size (Fig. 3(a)). The isotherm curve of the NS-LMO displays a well-defined step for the relative pressure P/P_o ranging from 0.6 to 0.8 as a typical IV classification with a clear H1-type hysteretic loop, which is characteristic of mesoporous materials [28]. The SS-LMO exhibits much smaller BET surface area of ~1.0 m^2 g^{-1} and no pore size distribution (Fig. 3(b)), as compared to the NS-LMO, resulting from particle agglomeration.

Fig. 4(a),(b) shows 1st charge-discharge curves of NS-LMO and SS-LMO at a current density of 1 C, respectively. At the cycling rate of 1 C, the 1st discharge capacities of NS-LMO and SS-LMO are ~96.19 and ~57.03 mAh g^{-1}, respectively. The NS-LMO exhibits much higher capacity during discharging process due to larger active sites for Li-ion intercalation and mesoporous structure facilitating lithium ions mobility compared to the SS-LMO.
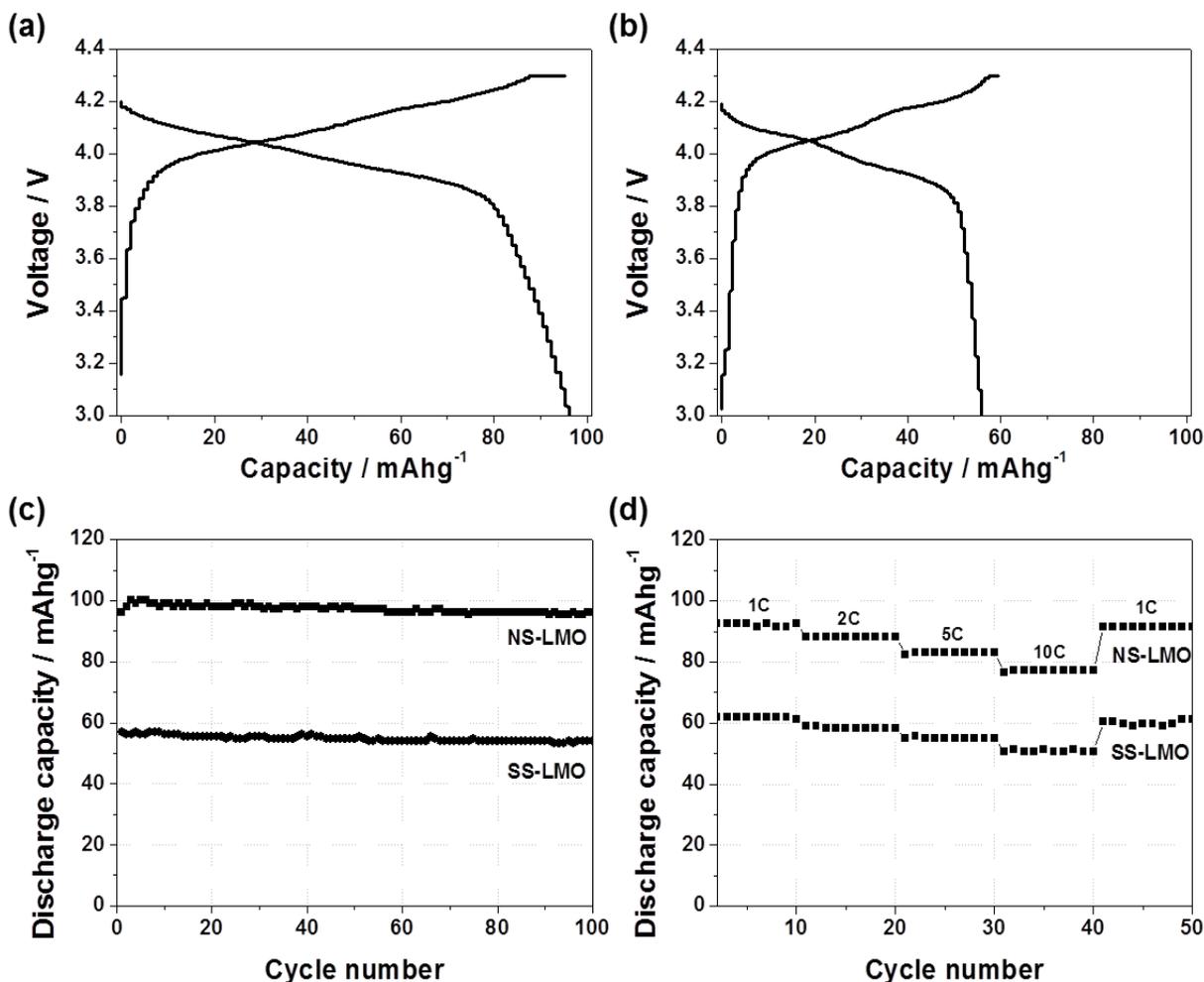
Figure 4. Charge-discharge curves of (a) NS-LMO and (b) SS-LMO at 1 C. (c) Cycle performance of NS-LMO and SS-LMO at 1 C for 100 cycles. (d) Rate cycling performance of NS-LMO and SS-LMO from 1 C to 10 C.

The discharge curve of the NS-LMO displays a smooth slope between 4.0 and 3.8 V whereas the SS-LMO displays a bent discharged region between 4.0 and 3.9 V, which might be mainly attributed to the lithium intercalation behavior of Mn_2O_3 as an impurity. The cycling performance of the NS-LMO and SS-LMO for 100 cycles at a current rate of 1 C is indicated in Fig. 4(c). The 10th discharge capacities of the NS-LMO and SS-LMO are ~99.05 and ~56.25 mAh g^{-1}, respectively. The 50th discharge capacities of the NS-LMO and SS-LMO are ~96.19 and ~53.90 mAh g^{-1}, respectively. After 100 cycles, the NS-LMO and SS-LMO show 100% and 94.5% capacity retention, respectively. To investigate the high C-rate cycling performance of the electrodes, the discharge-charge rates were increased stepwise from 1 to 10 C. As indicated in Fig. 4(d), the specific discharge capacities of the NS-LMO and SS-LMO are 89.91 and 62.50 mAh g^{-1} at 1 C; 88.24 and 59.03 mAh g^{-1} at 2 C; 83.19 and 54.86 mAh g^{-1} at 5 C; 77.31 and 50.69 mAh g^{-1} at 10 C, respectively. This represents that even at the increased current rates from 1 to 10 C, the NS-LMO can display an excellent high C-rate performance.

Nyquist plots of the NS-LMO and SS-LMO in the range between 100 kHz and 10 mHz are shown in Fig. 5(a). The value of the diameter of the semicircle on the Z_{real} axis is related to the charge transfer resistance (R_{ct}). The values of R_{ct} of the NS-LMO and SS-LMO are 200.5 and 629.5 Ω, respectively, representing much improved charge transport of the NS-LMO (Table 1). As indicated in Fig. 5(b), using the relationship between Z_{Re} and square root of frequency ($\omega^{-1/2}$) in the low frequency range (Eq. (1)) [34], the Warburg impedance coefficients (σ_W) of the NS-LMO and SS-LMO can be calculated to be 11.16 and 16.94 Ω cm^2 s$^{-1/2}$, respectively.
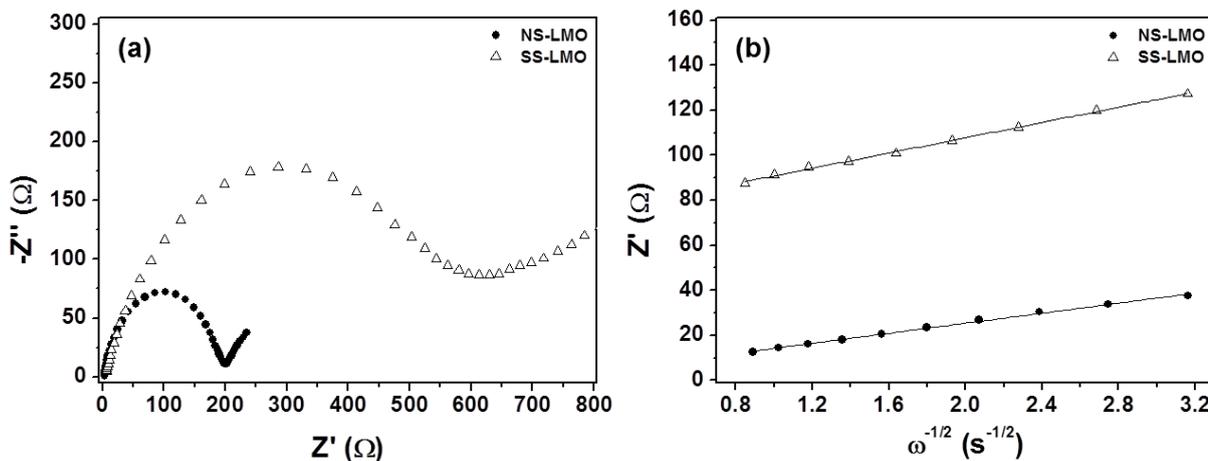
Figure 5. (a) Nyquist plots of NS-LMO and SS-LMO at 1 C in the frequency ranged between 100 kHz and 10 mHz.

Table 1. Comparison of charge transfer resistance (R_{ct}), Warburg impedance coefficient (σ_W), and diffusion coefficient (D) of the cathodes.

	R_{ct} / Ω	W / Ω cm^2 s$^{-1/2}$	D / cm^2 s^{-1}
NS-LMO	200.5	11.16	2.73×10^{-12}
SS-LMO	629.5	16.94	1.18×10^{-12}

$$Z_{Re} = R_e + R_{ct} + \sigma_W\, \omega^{-1/2} \tag{1}$$
$$D = R^2T^2 / 2A^2n^4F^4C^2\sigma_W{}^2 \tag{2}$$

From the Eq. (2), the Li-ion diffusion coefficients (D) of the NS-LMO and SS-LMO can be obtained to be 2.73×10^{-12} and 1.18×10^{-12} cm^2 s^{-1}, respectively, exhibiting faster Li-ion diffusion process in the NS-LMO in comparison with the SS-LMO. Aurbach and co-workers reported that D varies within 10^{-10} to 10^{-13} cm^2 s^{-1} [35]. As a result, the improved lithium-ion intercalation properties of the NS-LMO such as high capacity and high rate cycling performance may be attributed to relatively large specific surface area, low transport resistance, and high lithium ion diffusion coefficient in the mesoporous nanostructured electrode.

4. CONCLUSIONS

We have successfully synthesized the mesoporous NS-LMO nanostructured cathode material for high-performance lithium ion batteries using the PT method at relatively low reaction temperature. The NS-LMO prepared by the PT method with much higher surface area and mesoporous properties shows complete spinel LMO structure without any other phases, whereas the SS-LMO prepared by the SSR method consists of main LMO and extra phase of Mn_2O_3. The complete spinel structure, relatively large specific surface area, low transport resistance, and high lithium ion diffusion coefficient of the NS-LMO might lead to much higher capacity and improved cycling performance with complete retention compared to the SS-LMO.

References

1. B. Scrosati, *Nature*, 373 (1995) 557
2. J.-M. Tarascon and M. Armand, *Nature*, 414 (2001) 359
3. M. S. Whittingham, *MRS Bull.*, 33 (2008) 411
4. K. Kang, Y. S. Meng, J. Bréger, C. P. Grey and G. Ceder, Science, 311 (2006) 977
5. M. S. Whittingham, *Chem. Rev.*, 104 (2004) 4271
6. M. M. Thackeray, W. I. F. David, P. G. Bruce and J. B. Goodenough, *Mater. Res. Bull.*, 18 (1983) 461
7. E. Hosono, T. Kudo, I. Honma, H. Matsuda and H. Zhou, *Nano Lett.*, 9 (2009) 1045
8. J.-S. Kim, K. S. Kim, W. Cho, W. H. Shin, R. Kanno and J. W. Choi, *Nano Lett.*, 12 (2012) 6358
9. K. M. Shaju and P. G. Bruce, *Chem. Mater.*, 20 (2008) 5557
10. Y.-K. Sun and S.-H. Jin, *J. Mater. Chem.*, 8 (1998) 2399
11. A. S. Aricò, P. Bruce, B. Scrosati, J.-M. Tarascon and W. Van Schalkwijk, *Nat. Mater.*, 4 (2005) 366
12. C. Jiang, E. Hosono and H. Zhou, *Nano Today*, 1 (2006) 28
13. N. Kamarulzaman, R. Yusoff, N. Kamarudin, N. H. Shaari, N. A. Abdul Aziz, M. A. Bustam, N. Blagojevic, M. Elcombe, M. Blackford, M. Avdeev and A. K. Arof, *J. Power Sources*, 188 (2009) 274
14. W. Tang, X. J. Wang, Y. Y. Hou, L. L. Li, H. Sun, Y. S. Zhu, Y. Bai, Y. P. Wu, K. Zhu and T. Van Ree, *J. Power Sources*, 198 (2012) 308
15. J. Guan and M. Liu, *Solid State Ion.*, 110 (1998) 21
16. J.-H. Choy, D.-H. Kim, C.-W Kwon, S.-J. Hwang and Y.-I. Kim, *J. Power Sources*, 77 (1999) 1
17. B. J. Hwang, R. Santhanam and D. G. Liu, *J. Power Sources*, 97 (2001) 443
18. Y.-K. Sun, I.-H. Oh and K. Y. Kim, *Ind. Eng. Chem. Res.*, 36 (1997) 4839
19. M. Michalska, L. Lipińska, M. Mirkowska, M. Aksienionek, R. Diduszko and M. Wasiucionek, *Solid State Ion.*, 188 (2011) 160
20. Y. Zhang, H.-C. Shin, J. Dong and M. Liu, *Solid State Ion.*, 171 (2004) 25
21. C.-Z. Lu and T.-K. Fey, *J. Phys. Chem. Solids*, 67 (2006) 756
22. A. R. Naghash and J. Y. Lee, *J. Power Sources*, 85 (2000) 284

23. W. Tang, L. L. Liu, S. Tian, L. Li, L. L. Li, Y. B. Yue, Y. Bai, Y. P. Wu, K. Zhu and R. Holze, *Electrochem. Commun.*, 13 (2011) 1159
24. R. Jiang, C. Cui and H. Ma, *Mater. Lett.*, 91 (2013) 12
25. A. Navulla, L. Huynh, Z. Wei, A. S. Filatov and E. V. Dikarev, *J. Am. Chem. Soc.*, 134 (2012) 5762
26. Y.-L. Ding, J. Xie, G.-S. Cao, T.-J. Zhu, H.-M. Yu and X.-B. Zhao, *Adv. Funct. Mater.*, 21 (2011) 348
27. T. J. Patey, R. Büchel, M. Nakayama and P. Novák, *Phys. Chem. Chem. Phys.*, 11 (2009) 3756
28. J.-Y Luo, Y. Wang, H.-M. Xiong, and Y.-Y Xia, *Chem. Mater.*, 19 (2007) 4791
29. M. B. Zakaria, N. Suzuki, N. L. Torad, M. Matsuura, K. Maekawa, H. Tanabe and Y. Yamauchi, *Eur. J. Inorg. Chem.*, 13 (2013) 2330
30. G. J. Soler-Illia, A. A. De, C. Sachez, B. Lebeau, and J. Patarin, *Chem. Rev.*, 102 (2002) 4093
31. M. W. Raja, S. Mahanty and R. N. Basu, *Solid State Ion.*, 180 (2009) 1261
32. H. W Chan, J. G. Duh and S. R. Sheen, *J. Power Sources*, 115 (2003) 110
33. W. Sun, F. Cao, Y. Liu, X. Zhao, X. Liu and J. Yuan, *J. Mater. Chem.*, 22 (2012) 20952
34. B. Pei, H. Yao, W. Zhang and Z. Yang, *J. Power Sources*, 220 (2012) 317
35. D. Aurbach, M. D. Levi, E. Levi, H. Teller, B. Markovsky and G. Salitra, *J. Electrochem. Soc.*, 145 (1998) 3024